

Preparation and Capacity-Fading Investigation of Polymer-Derived Silicon Carbonitride Anode for Lithium-Ion Battery

Yan Feng,*^{†,§} Shuming Dou,[‡] Yuzhen Wei,[†] Yuliang Zhang,[†] Xiangyun Song,[§] Xifei Li,*^{‡,||} and Vincent S. Battaglia[§]

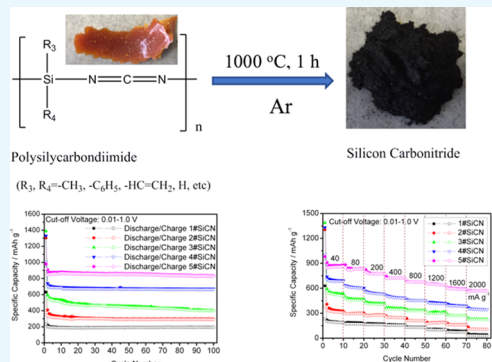
[†]College of Chemistry and [‡]College of Physics and Materials Science, Tianjin Normal University, Tianjin 300387, P. R. China

[§]Energy Storage and Distributed Resources Division, Lawrence Berkeley National Laboratory, Berkeley, California 94720, United States

^{||}Institute of Advanced Clean Energy, Xi'an University of Technology, Xi'an 710048, P. R. China

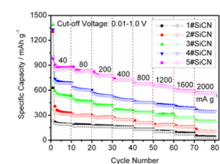
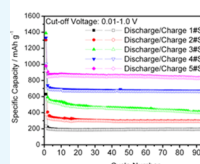
S Supporting Information

ABSTRACT: Polymer-derived silicon carbonitride (SiCN) materials have been synthesized via pyrolyzing from five poly(silylcarbodiimide)s with different contents of carbon (labeled as 1–5#). The morphological and structural measurements show that the SiCN materials are mixtures of nanocrystals of SiC, Si_3N_4 , and graphite. The SiCN materials have been used as anodes for lithium-ion batteries. Among the five polymer-derived SiCN materials, 5#SiCN, derived from dichloromethylvinylsilane and di-*n*-octyldichlorosilane, has the best cycle stability and a high-rate performance at the low cutoff voltage of 0.01–1.0 V. In lithium-ion half-cells, the specific delithiation capacity of 5#SiCN anode still remains at $826.7 \text{ mA h g}^{-1}$ after 100 charge/discharge cycles; it can even deliver the capacity above 550 mA h g^{-1} at high current densities of 1.6 and 2 A g^{-1} . In lithium-ion full cells, 5#SiCN anode works well with $\text{LiNi}_{0.6}\text{Co}_{0.2}\text{Mn}_{0.2}\text{O}_2$ commercial cathode. The outstanding electrochemical performance of 5#SiCN anode is attributed to two factors: (1) the formation of a stable and compact solid electrolyte interface layer on the anode surface anode, which protects the electrode from cracking during the charge/discharge cycle; and (2) a large amount of carbon component and the less Si_3N_4 phase in the 5#SiCN structure, which provides an electrochemical reactive and conductive environment in the SiCN structure, benefit the lithiation/delithiation process. In addition, we explore the reason for the capacity fading of these SiCN anodes.



Polysilylcarbodiimide

($R_3, R_4 = \text{CH}_3, \text{-C}_6\text{H}_5, \text{-HC}=\text{CH}_2, \text{H}$, etc)



1. INTRODUCTION

As one of the promising candidate for new energy storage devices, lithium-ion batteries (LIBs) have received considerable attention and have been widely applied in portable devices and power tools such as electric equipment and electric/hybrid vehicles because they can potentially fulfill the requirements of high energy density, high efficiency, and low emission simultaneously.^{1–3} Nevertheless, the conventional graphite anode is characterized by low capacity (372 mA h g^{-1} in theory) and low kinetics at a high charge/discharge rate, which is unable to achieve the increasing requirement for LIBs with higher capacity and better rate performance in high-energy and high-power density applications.^{4,5}

Polymer-derived silicon carbonitride (SiCN) materials have emerged as one of the promising alternative anode materials in the last decade.^{6,7} They are prepared by the pyrolysis of organic polymers containing Si, H, C, and N in an inert atmosphere at 1000–1600 °C. After organic–inorganic transition in the pyrolysis, amorphous SiCN structure, which consists of graphene-like carbon chains wrapped around nanosized domains of silicon nitride and silicon carbide, is obtained. SiCN has unique Si–C, Si–N, and Si–C–N network structures

with embedded numerous dangling bonds of silicon, free carbon (amorphous carbon), and graphene sheets. Lithium ion can bond with those silicon and carbon atoms to deliver a high reversible capacity of $400\text{--}800 \text{ mA h g}^{-1}$, which is better than that of the current graphite anodes.^{8–12} Sanchez-Jimenez et al. reported that the silicon-based mixed bond of silicon oxycarbide (SiOC) in a tetrahedra sequesters an equivalent of $\sim 50\,000 \text{ mA h g}^{-1}$ -atom, whereas “free carbon” can sequester $\sim 5000 \text{ mA h g}^{-1}$ -atom for the reversible portion of the lithium insertion.¹³ Additionally, Fukui et al. confirmed by ^{7}Li NMR that the Si–O–C composite material electrochemically stores lithium species in interstitial spaces or edges of the graphene layers, the Si–O–C glass phase, and the micropores.¹⁴ These SiOC materials have a similar structure as our SiCN materials,^{6,7} which suggests the big potential for the high reversible capacity of our SiCN materials.

Although the SiCN anode has many advantages for lithium-ion battery, its irreversible capacity in the first few cycles is low

Received: September 30, 2017

Accepted: November 8, 2017

Published: November 17, 2017

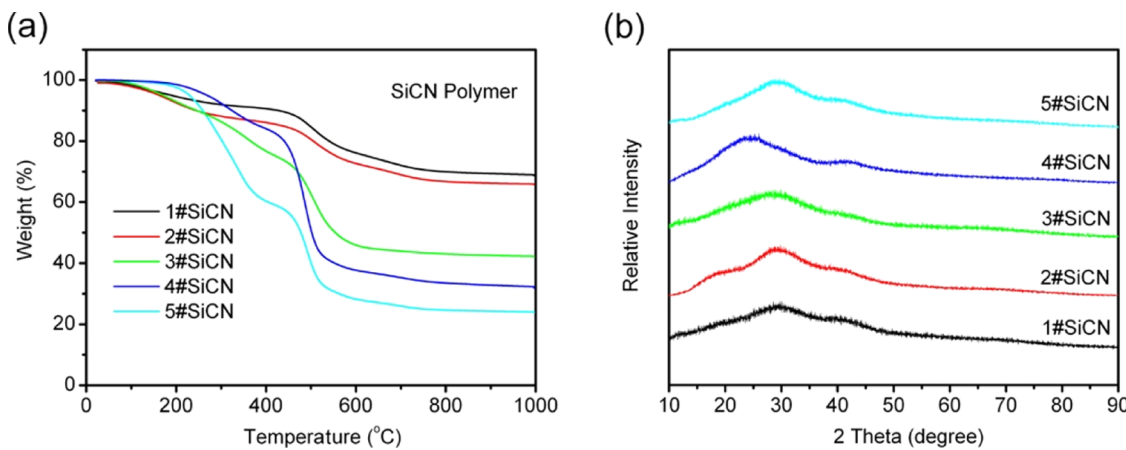


Figure 1. (a) TGA analysis of the cross-linked SiCN polymer precursors. (b) XRD patterns of the 1–5#SiCN materials after pyrolysis.

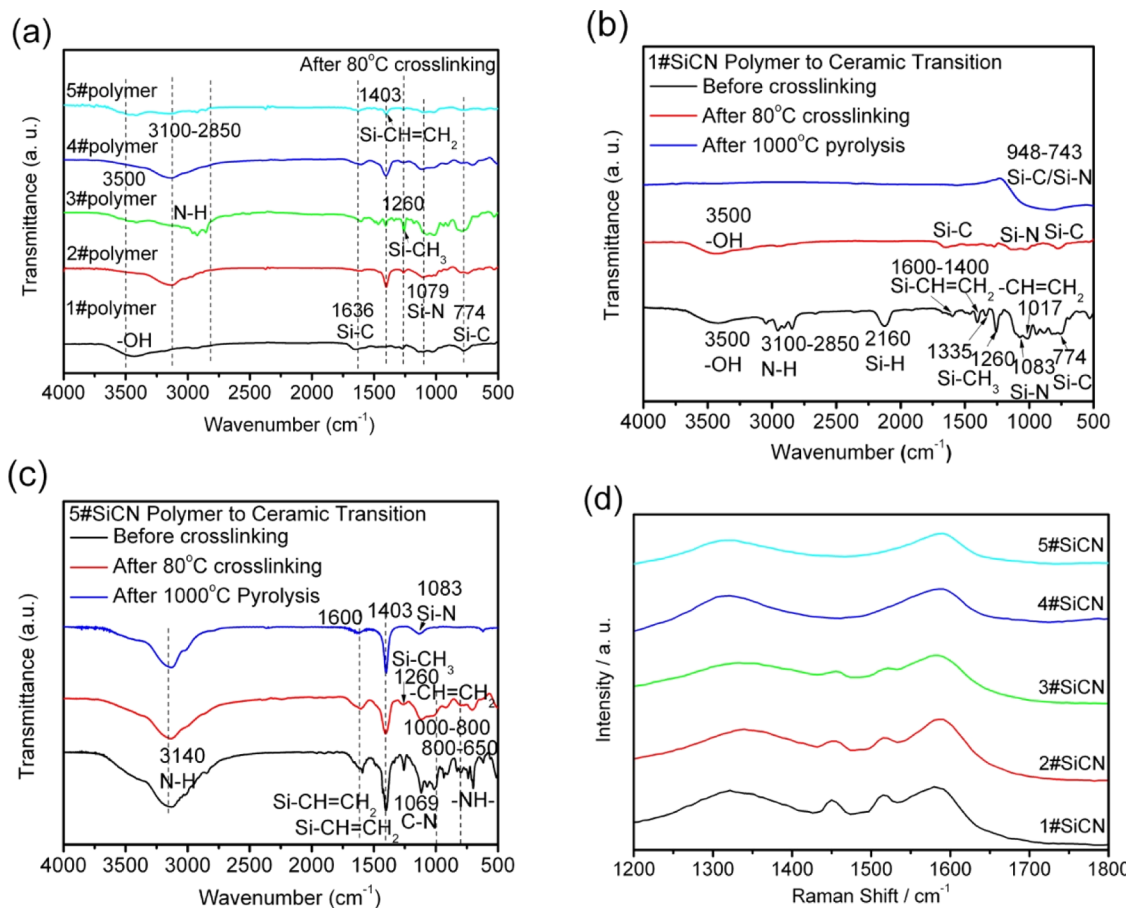


Figure 2. (a) FTIR spectra of 1–5#SiCN polymer precursors after 80 °C cross-linking. (b) FTIR spectra of 1#SiCN polymer before cross-linking, after 80 °C cross-linking, and after 1000 °C pyrolysis. (c) FTIR spectra of the 5#SiCN polymer before cross-linking, after 80 °C cross-linking, and after 1000 °C pyrolysis. (d) Raman spectra of 1–5#SiCN materials after 1000 °C pyrolysis.

(40–50%) due to its low electrical conductivity and the volume expansion during charge–discharge cycle.^{15,16} To resolve this issue, increasing the carbon content in the SiCN matrix is an efficient way to improve the integral conductivity of SiCN. Two strategies have been implemented to improve the carbon content in SiCN: first, coat or incorporate carbon materials; second, use carbon-rich polymer for pyrolysis. In previous work, our group has incorporated carbon materials such as graphite,¹⁷ carbon nanotubes,¹⁸ and graphene¹⁹ into SiCN. With increasing carbon content in the SiCN/carbon

composites, the cycle stability and high rate performance have been dramatically improved by 2–6 times. In addition, the same results have been found by other research groups.^{20–24} The latter strategies employ a carbon-rich preceramic derivation such as polyphenylvinylsilylcarbodiimide,^{25–28} polyphenylvinylsilazane,^{29,30} and divinylbenzene^{31,32} as the precursors for pyrolysis. Due to the high carbon content in the precursor, the final products can exhibit a high carbon content. Nevertheless, there are significant differences between the two strategies. The former needs at least two steps: pyrolysis of

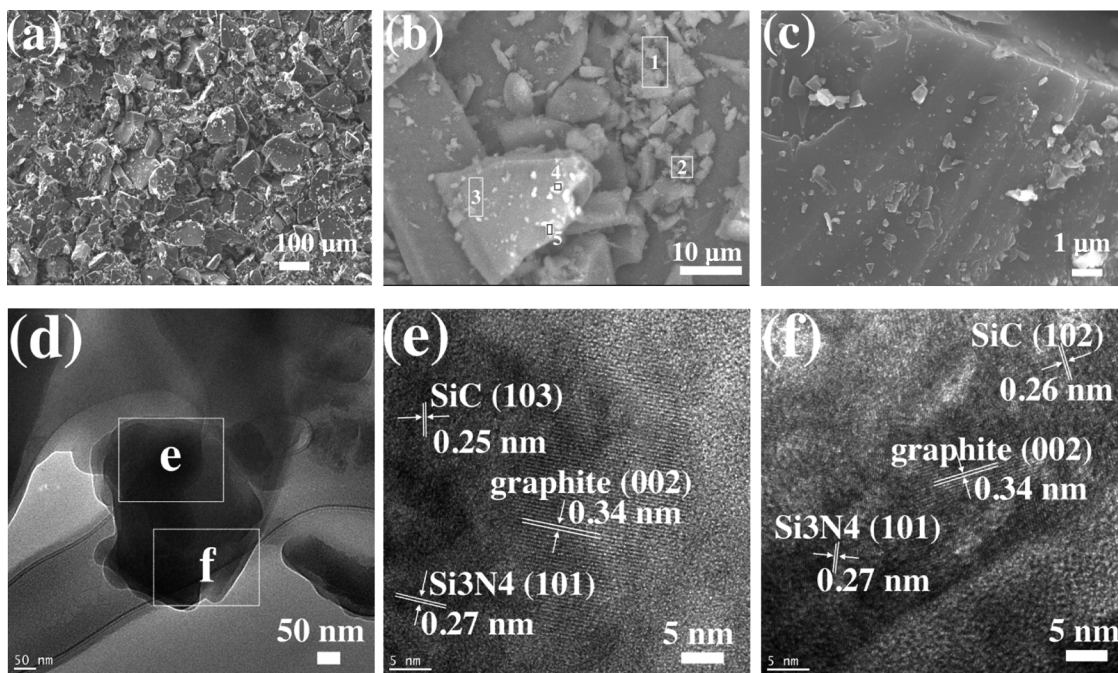


Figure 3. Scanning electron microscopy (SEM) images (a–c) and TEM images (d–f) of 5#SiCN materials.

polymer to obtain SiCN followed by another heat treatment to incorporate carbon materials in SiCN. The latter is easier and more beneficial because all of the preparations are in one step in which the achievement of a carbon-rich preceramic polymer is an important factor.

Herein, we adopt carbon-rich polymer precursors with different carbon containing to fabricate SiCN materials and then test the electrochemical performances of these SiCN anodes both in lithium-ion half cells and full cells. Moreover, we further explore the reason for the capacity fading of these SiCN anodes. With different element contents of silicon, carbon, and nitrogen in the final products, the SiCN material would show different nanosized domains in the matrix, which effects their electrochemical performances. The purpose of this work is to investigate the carbon contribution in SiCN material for reversible lithiation/delithiation process, accordingly we can illustrate the inter-relation between the polymer and the final SiCN material to further optimize the carbon-rich SiCN structure for excellent electrochemical performance.

2. RESULTS AND DISCUSSION

2.1. Structure and Morphology. The detailed syntheses of 1–5#SiCN materials are given in [Experimental Section](#). [Figure 1a](#) shows the thermogravimetric analysis (TGA) analysis of the cross-linked SiCN polymer precursor. As indicated by the TGA curves, the weight loss observed below 250 °C most likely corresponds to the loss of water due to desorption of physically absorbed water on the materials.^{33,34} The different weight losses in the five cross-linked SiCN polymers, poly(silylcarbodiimide), at the temperature interval of 250–800 °C indicate the different decomposition statuses due to the variety of organic groups and the carbon framework from the five polymers. In the pyrolysis process, the polymer precursors are transformed from organic phase to inorganic phase.^{35,36} For our polymer samples, all of the polymers changed into inorganic compounds at the temperature above 800 °C. The different phase transformation at the temperature 250–600 °C

may cause a different chemical composition in the resulting SiCN products. X-ray diffraction (XRD) was employed to further investigate the structure of SiCN materials after pyrolysis, as shown in [Figure 1b](#). As shown in the XRD patterns, the diffraction peaks of five SiCN samples are broad, suggesting amorphous structures. Because these large amounts of amorphous phases may be covered by the low nanocrystals in the SiCN structures, we cannot ensure the specific structures of the SiCN samples. To solve the issues, the following Fourier transform infrared (FTIR) spectroscopy and transmission electron microscopy (TEM) analysis are carried out for further investigation.

[Figure 2a](#) shows the FTIR spectra of 1–5#SiCN polymer precursors after 80 °C cross-linking. As shown, the five SiCN polymers consist of many organic groups such as –OH, N–H, Si–H, Si–N, Si–C, and Si–CH=CH₂. It is noted that the number and IR intensity of organic groups depend on the characteristics and constituents of different polymers. To further explore, we choose two polymers, 1# and 5#SiCN, as examples to investigate their FTIR spectra before and after 80 °C cross-linking and after 1000 °C pyrolysis, as shown in [Figure 2b,c](#), respectively. As shown in [Figure 2b](#), before cross-linking, the 1#SiCN precursor has many organic groups, including –OH, N–H, Si–H, Si–CH=CH₂, Si–CH₃, –CH=CH₂, Si–N, and Si–C. During the cross-linking process, the breakage of double bonds of Si–CH=CH₂ and –CH=CH₂ indicated that the organic monomers were transferred into polymers. In the following pyrolytic process, the polymer was transferred into a ceramic, which involved the breaking of Si–CH₃ and C–H bonds. This transformation was clearly recorded in the FTIR spectra, with a decrease in the intensity of the corresponding peaks. Finally, the pyrolyzed 1#SiCN sample does not have any organic groups. The same phenomenon was also found in 5#SiCN ([Figure 3c](#)), except that a small quantity of Si–CH=CH₂ still existed in the sample, which indicated incomplete cross-linking and pyrolysis. From [Figure 2a](#), we can see that an increase in the amount of

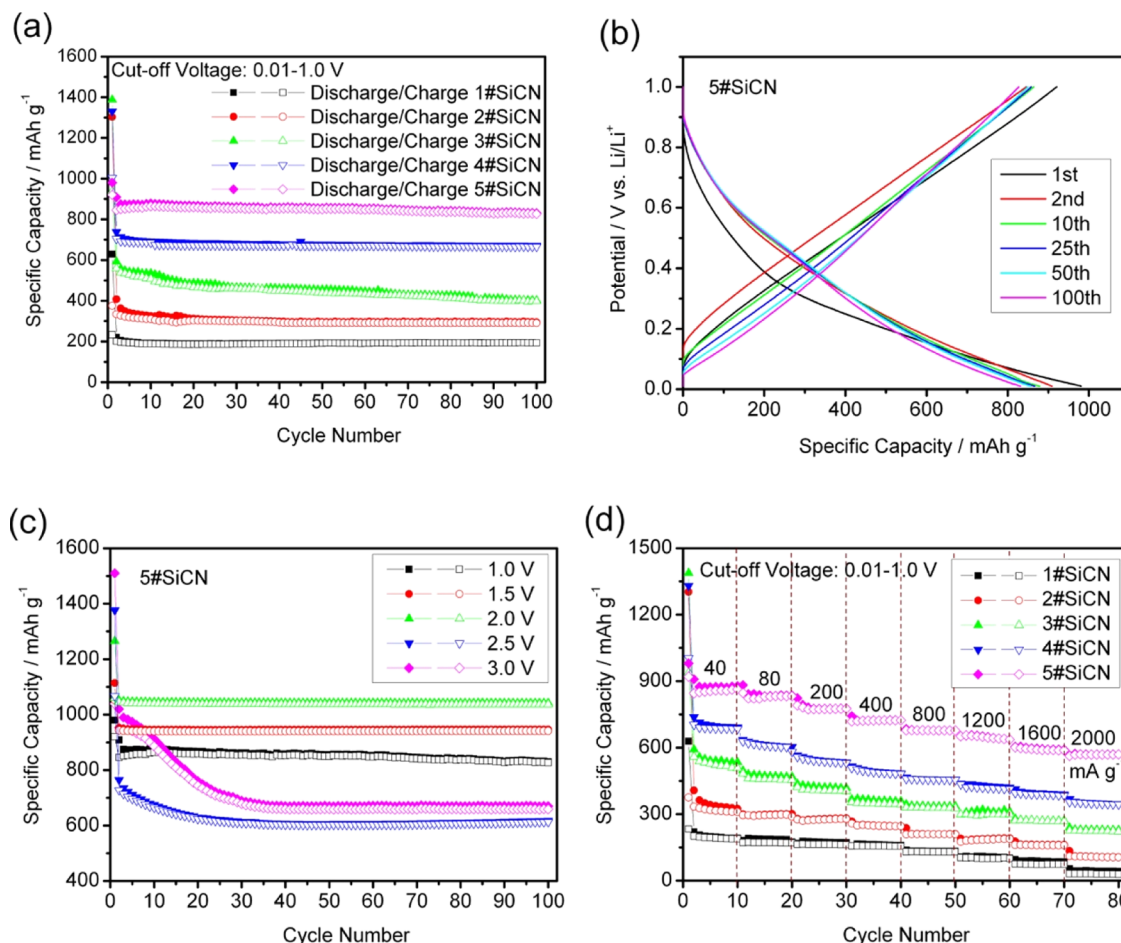


Figure 4. (a) Cycle performances of 1–5#SiCN anodes at the current density of 40 mA g^{-1} with the cutoff voltage of 0.01–1.0 V. (b) The specific capacity–potential curves of the 1st, 2nd, 10th, 25th, 50th, and 100th charge/discharge cycles of 5#SiCN anode at the current density of 40 mA g^{-1} with the cutoff voltage of 0.01–1.0 V. (c) Cycle performances of 5#SiCN anode at the current density of 40 mA g^{-1} and the cutoff voltages of 0.01–1.0, 1.5, 2.0, 2.5, and 3.0 V. (d) High-rate performances of 1–5#SiCN anodes at the charge/discharge current densities of 40, 80, 200, 400, 800, 1200, 1600, and 2000 mA g^{-1} (all in half-cells).

the double bonds in polymers after cross-linking from sample 1–5 indicates a decrease in the extent of cross-linking. This is due to an increase in the molecular mass of the monomers involved in the cross-linking process, leading to more difficulty in proceeding with the cross-linking reaction.

To further reveal the structure of 1–5#SiCN synthesized from different carbon-containing polymers, the nature of the carbon obtained in the SiCN samples is worth studying. We employ Raman spectroscopy to reveal the graphitic and amorphous carbon content in the SiCN materials. As shown in Figure 2d, the 1–5#SiCN materials show two major characteristic bands in the Raman shift from 1200 to 1800 cm^{-1} : the G band at 1590 cm^{-1} and the D band at 1320 cm^{-1} . It is known that the G band is the response of the inplane stretching motion of the symmetric sp^2 C–C band, whereas the D band results from the disruption and defects of the symmetrical hexagonal graphitic lattice. The increase in the intensity ratio of D band and G band ($I_{\text{D}}/I_{\text{G}}$) from 1 to 5#SiCN (0.8621, 0.8917, 0.9421, 0.9552, and 0.9555) indicates a decrease in the size of sp^2 domains and an increase in the defects in the graphitic lattice. That is, the ratio of amorphous carbon increased in the relevant SiCN products, whereas the content of graphitic carbon decreased in them, with the initial carbon ratio increasing from 1 to 5# polymer precursor.

The morphologies of SiCN materials are characterized by SEM in Figure 3a–c. As shown in Figures 3a and S2 of the Supporting Information, 1–5#SiCN materials are composed of massive irregularly blocked particles with dense and rigid surfaces. These particles are of nonuniform sizes and distributed between 10 and 100 μm . In the enlarged SEM images (Figure 4b,c), it is clear that a lot of small particles are dispersed randomly on the large particles. We analyzed five different areas of this small particles in Figure 3b, which are marked as numbers 1–5 in the energy-dispersive X-ray (EDX) spectrum. The EDX results are shown in Table 1. The EDX results based on areas 1–3 and 5 indicate that the most component of these small particles are carbon, with slight amounts of silicon and chlorine. However, the EDX result

Table 1. Carbon Content of 1–5#SiCN Materials by EDX Analysis

area number	Si/wt %	C/wt %	Cl/wt %
1	2.51	97.38	0.12
2	1.87	98.05	0.09
3	3.28	96.48	0.24
4	94.13		5.87
5	3.13	96.75	0.12

based on area 4 illustrated that the small particle can be mixed substances of silicon nanocrystal and silicon chloride. Briefly, all of the EDX results reveal that the small particles on the surface of large particle in SiCN material are mainly carbon and silicon substances without nitrogen ingredient.

Because the EDX analysis of the 5#SiCN material does not accurately reflect the macroscopic carbon content in the whole composite, we employ carbon analysis using a Vario El Cube analyzer. The carbon analysis data are listed in Table 2. As

Table 2. Chemical Compositions of 1–5#SiCN Materials Determined by Element Analysis

samples	C/wt %	N/wt %	H/wt %
1#SiCN	4.33	1.68	0.86
2#SiCN	7.67	1.87	0.85
3#SiCN	13.05	2.87	1.05
4#SiCN	17.73	4.81	1.48
5#SiCN	49.15	1.14	1.89

shown, 5#SiCN has the highest carbon weight percentage because the polymer precursor (raw reaction material) of 5#SiCN has the highest carbon content. The carbon weight percentages increases from 1 to 5#SiCN.

However, we employ TEM for further investigation because the structure of SiCN cannot be completely demonstrate by XRD. Areas (e) and (f) (Figure 3d) are chosen for high-resolution TEM analysis, which is shown in Figure 3e,f, respectively. The crystal lattices of SiC, Si_3N_4 , and graphite show that SiCN material is mainly a mixture of these three crystals. Because of the low crystallinity of the SiC, Si_3N_4 , and graphite crystals that may be covered by large amounts of amorphous phases, SiC and Si_3N_4 phases are not found in the XRD pattern (Figure 1b).

2.2. Electrochemical Performances. The electrochemical performances of SiCN–graphene composite as anodes in Li-ion batteries are shown in Figures 4–5. Figure 4a shows the cycle performances of 1–5#SiCN anodes at the current density of 40 mA g^{-1} and cutoff voltage of 0.01–1.0 V. After 100 charge and discharge cycles, the specific delithiation capacities of the SiCN anodes in the order of increasing label number remained at 193.2, 290.6, 398.2, 665.5, and 826.7 mA h g^{-1} . Except for the first two cycles, the Coulombic efficiency of all of the SiCN anodes was above 97% (Figure S3 of the Supporting

Information). Although the Coulombic efficiency of the first cycle was not satisfied, the numerical value of Coulombic efficiency increased from 28.2 to 75.5% from 1 to 5#SiCN, indicating outstanding performance of the 5#SiCN anode. The low Coulombic efficiency in the first few charge–discharge cycles, which can often be found in many Si-based anodes in the lithium-ion battery, was caused by the large volume expansion during the lithiation–delithiation process, which caused serious pulverization and delamination.^{37,38} After the first two cycles, the capacity of all of the 1–5#SiCN anodes is kept stable, showing no phenomenon of capacity decay; this is because the active materials of SiCN anodes become stable and electrochemically reversible after the first two cycles.

Figure 4b shows the charge and discharge potential curves vs capacity for the 5#SiCN anode at the 1st, 2nd, 10th, 25th, 50th, and 100th charge/discharge cycles. The slow slopes of charge–discharge potential curves without any distinct potential plateaus indicate an amorphous structure of the oxidation–reduction sites available for the insertion and extraction of Li ions, which is consistent with their XRD patterns in Figure 1b.

As known, to obtain the available voltage gap between the cathode and anode in lithium-ion full-cells, the anode must work at low voltages. Therefore, our SiCN anodes are tested under different cutoff voltages in half-cells to predict the capability in full-cells. Figure 4c shows the cycle performance of 5#SiCN anode under the same charge and discharge conditions with different cutoff voltages. As shown, the specific reversible capacities of the 5#SiCN anode are approximately 826.7, 941.1, 1037.1, 612.5, and 658.7 mA h g^{-1} corresponding to the cutoff voltage ranges of 0.01–1.0, 1.5, 2.0, 2.5, and 3.0 V, respectively. At lower cutoff voltages (1.0 and 1.5 V), the 5#SiCN has a better cycle stability. However, at higher cutoff voltages (2.0, 2.5, and 3 V), it has the worst cycle stability because the number of the lithium-ion insertion/deinsertion at the higher cutoff voltage is much more than that at the lower cutoff voltage. Thus, more structural damage may occur in the anode at the higher cutoff voltage, resulting in capacity fading. Figure 4c reveals that even at the low cutoff voltage of 0.01–1.0 V, the 5#SiCN anode can still deliver a high reversible capacity of over 820 mA h g^{-1} , which is qualified as an anode material in Li-ion full-cells.

Figure 4d shows the high-rate performance of 1–5#SiCN anodes at different current densities between the cutoff voltage of 0.01 and 1.0 V. Among them, 5#SiCN anode exhibits the

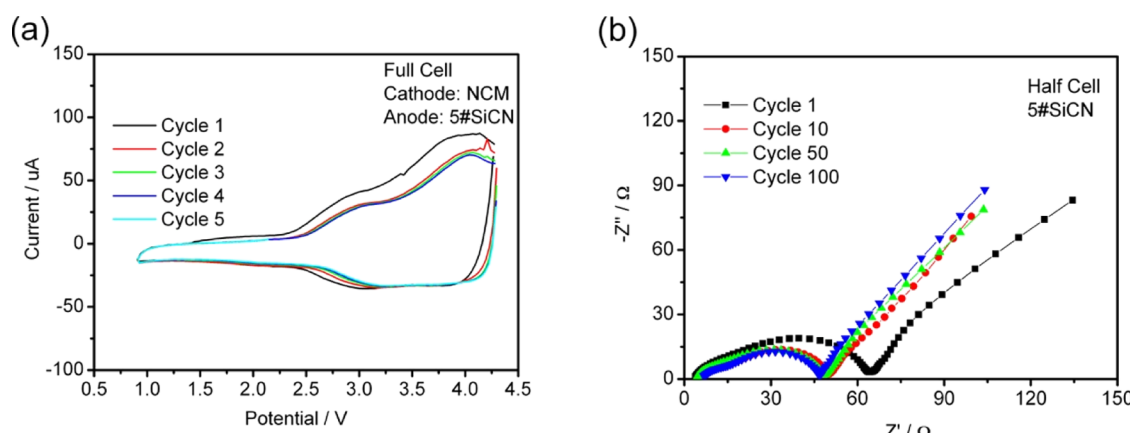


Figure 5. (a) Cyclic voltammetry curves of NCM cathode/5#SiCN anode in a full-cell (NCM cathode). (b) EIS Nyquist plots of experimental data of 5#SiCN anodes in a half-cell.

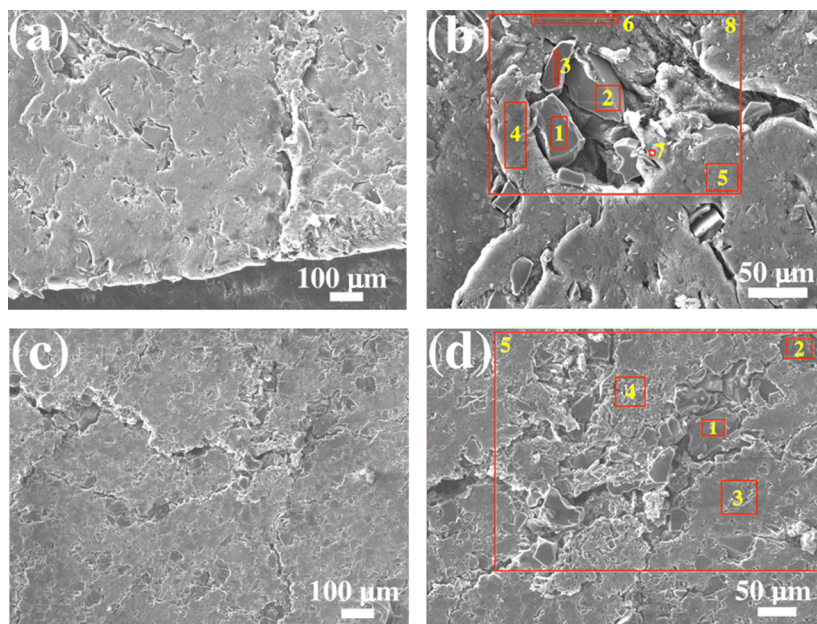


Figure 6. SEM images of 5#SiCN anode before (a, b) and after 100 charge/discharge cycles (c, d). Inserted numbers in (b) and (d) are EDX analysis areas.

best performance, delivering the highest capacity of about 863.8, 833.0, 776.5, 724.2, 677.8, 637.2, 588.4, and 569.6 mA h g⁻¹ at each of the applied current densities of 40, 80, 200, 400, 800, 1200, 1600, and 2000 mA g⁻¹, respectively. This excellent high-rate performance of SiCN anodes is very attractive in LIBs.

We employ full-cells to investigate the voltage window of our SiCN anode. The SiCN electrode is used as an anode and the LiNi_{0.6}Co_{0.2}Mn_{0.2}O₂ (NCM cathode, type 622, SamSung Company) is used as the cathode. The lithium-ion electrolyte and cell separator were the same as that of the half-cells. The cyclic voltammetry (CV) profiles of NCM/5#SiCN in a full-cell at the scan rate of 0.05 mV s⁻¹ for the first five scanned cycles are shown in Figure 5a. There are wide reduction peaks at around 3.0 and 4.0 V and an oxidation peak at 3.2 V, suggesting that our NCM/5#SiCN full-cell could work well. Moreover, the five cycle curves could almost coincide, indicating that the NCM/5#SiCN full-cell could exhibit stable capacity during lithiation/delithiation cycles. As shown in Figure 5b, electrochemical impedance spectroscopy (EIS) test is carried out to evaluate the electrochemical kinetics properties of our best-performance 5#SiCN anode in a half-cell at the 1st, 10th, 50th, and 100th charge/discharge cycle. Each Nyquist plot of cycle 1–100 consists of a high-to-medium frequency-depressed semicircle and a low-frequency straight line, corresponding to the charge-transfer resistance representing the electrode reaction kinetics, and a Warburg resistance associated with the diffusion process of lithium ions in the electrode.^{35,36} After the extended cycling from 1 to 10 cycles, the charge-transfer resistance of the 5#SiCN decreased tremendously. The decrease is ascribed to the loss of active materials upon cycling, which leads to the capacity decay. With continued cycling from 10 to 100 cycles, the charge-transfer resistance remains unchanged, evidencing the stability of the electrode after first 10 cycles. That phenomenon matches well with the charge/discharge cycling performance shown in Figure 4a.

2.3. Theoretical Capacity. For further understanding of the SiCN composites, we calculate the theoretical capacity and

speculate the corresponding lithiation/delithiation reaction. Our SiCN composite is mainly the mixture of SiC, Si₃N₄, and graphite crystals, which is proved by TEM (Figure 3e,f). Accordingly, the lithiation/delithiation capacity of our SiCN composite is mainly attributed to the SiC, Si₃N₄, and graphite. When they react with Li completely, SiC reacts with Li to form Li_{4.4}Si and LiC₆, and Si₃N₄ reacts with Li to form Li_{4.4}Si and Li₃N. The lithiation/delithiation equations are as follows



That is to say, the numbers of electrons transferred (*n*) in the two equations are 4.57 per mol SiC and 25.2 per mol Si₃N₄, respectively. According to the formula of theoretical capacity

theoretical capacity of active material

$$= \frac{F \times n}{3.6 \times M} (\text{mA h g}^{-1})$$

where *F* is the Faraday constant, *n* is the number of electrons transferred in the lithiation/delithiation reaction, and *M* is the molecular weight of active material. Therefore

theoretical capacity of SiC

$$= \frac{96\ 500 \times 4.57}{3.6 \times 40.10} \\ = 3055 \text{ mA h g}^{-1}$$

theoretical capacity of Si₃N₄

$$= \frac{96\ 500 \times 25.2}{3.6 \times 140.27} \\ = 4816 \text{ mA h g}^{-1}$$

As known, the theoretical capacity of graphite is 372 mA h g⁻¹. The total theoretical capacity of the composite is equal to the sum of the theoretical capacity of above three components

multiplied by their respective weight ratio in the SiCN composite.

Herein, we can estimate the theoretical capacity of the SiCN composite by a simple mathematic calculation. Take 5#SiCN as an example. To explore the weight percentage of Si-based compound (mainly SiC and Si_3N_4) and graphite, we employ SEM and EDX analyses to compare the chemical components in the anodes before and after charge/discharge cycles. Figure 6 shows the SEM images of 5#SiCN anode before and after 100 charge/discharge cycles. Tables 3 and 4 are the corresponding

Table 3. Element Weight Percentages of 5#SiCN Anode before Charge/Discharge Cycle by EDX Analysis

area number	Si/wt %	C/wt %	O/wt %	F/wt %	Cl/wt %
1	24.75	46.40	28.85		
2	24.00	48.90	25.36	1.55	0.19
3	17.71	70.26	12.03		
4	2.78	83.20		14.02	
5	2.90	83.34		13.76	
6	1.93	84.35		13.72	
7	5.05	71.38	15.66	7.91	
8	6.59	74.89	7.44	11.08	

Table 4. Element Weight Percentages of 5#SiCN Anode after 100 Charge/Discharge Cycles by EDX Analysis

area number	Si/wt %	C/wt %	O/wt %	F/wt %	P/wt %	Cl/wt %
1	18.19	32.10	24.80	22.54	2.37	
2	19.06	26.76	22.63	27.87	3.55	0.12
3	12.24	36.52	21.18	26.48	3.25	
4	10.81	31.06	24.07	27.99	4.60	
5	11.93	35.11	22.29	26.76	3.60	

element weight percentages of 5#SiCN anode before and after 100 charge/discharge cycles. From Tables 3 and 4, the weight percentages of Si-base compound in the 5#SiCN composite electrode is approximately 22 wt % before cycling and 14 wt % after cycling. We suppose that the average capacity of Si-based compounds (SiC and Si_3N_4) in the composite is $(3055 + 4816)/2 = 3935.5 \text{ mA h g}^{-1}$. Hence, the initial capacity (before cycling) of the SiCN composite = $(3935.5 \times 22\%) + (372 \times 78\%) = 1156 \text{ mA h g}^{-1}$; the reversible capacity (after cycling) of the SiCN composite = $(3935.5 \times 14\%) + (372 \times 86\%) = 871 \text{ mA h g}^{-1}$.

This calculated capacity of the SiCN composite properly matches its actual reversible capacity. As shown in Figure 4a, the actual reversible capacity of our 5#SiCN electrodes is $\sim 830 \text{ mA h g}^{-1}$ after 100 charge/discharge cycles. However, because the weight ratio of Si-based compounds and graphite is different in the final composites, the reversible capacities of 1–5#SiCN samples vary from ~ 200 to 830 mA h g^{-1} .

2.4. Capacity-Fading Analysis. To further explore why 5#SiCN has the best extraordinary electrochemical performance among the five SiCN anodes, we compare its chemical components before and after charge/discharge cycles. Before cycling (Figure 6a), the SiCN particles are embedded into the carbon black powder to form a flat and homogeneous electrode surface. After cycling (Figure 6c), the electrode surface has no big changes. The SiCN particles maintain good contact with the conductive material, the carbon black powder, to ensure electronic conductivity of the active material in the electrode, in turn, decreasing the capacity decay of the 5#SiCN anode. In

Figure 6b,d, the inserted rectangular frames with numbers are the areas analyzed by EDX. Tables 3 and 4 are the element weight percentages of 5#SiCN anode before and after 100 charge/discharge cycles, respectively. Before cycling, the areas 1–3 in Figure 6b are mainly composed of silicon, carbon, oxygen, and slight amounts of fluorine and chlorine. The areas 4–7 in Figure 6b are mainly composed of carbon, oxygen, fluorine, and slight amount of silicon, indicating that the areas 1–3 are SiCN particles and the areas 4–7 mainly are carbon black. After 100 charge/discharge cycles, the areas 1 and 2 in Figure 6d represent the active material (SiCN particles), whereas areas 3 and 4 represent the conductive material (carbon black). Chlorine is the complete reacted reagents in the synthetic process. Oxygen, fluorine, and phosphorus (Table 4) come from the solid electrolyte interfaces (SEIs) layer that was formed during the charge/discharge cycle. The element weight percentages in area 8 of Figure 6b and area 5 in Figure 6d represent the total element distribution based on the large surface area of the electrode. In comparison, the contents of silicon and carbon of SiCN particle in the electrode are decreased, whereas the contents of oxygen, fluorine, and phosphorus in the electrode are increased. The same tendency is also exhibited in the area of carbon black, indicating the formation of stable and compact SEI layer on the surface anode protects the electrode cracking during the charge/discharge cycle, resulting in decrease in the capacity decay.

To investigate the possible capacity decay mechanism of the SiCN anodes, XRD characterization of the anode materials is performed after electrochemical testing. Figure 7 shows the

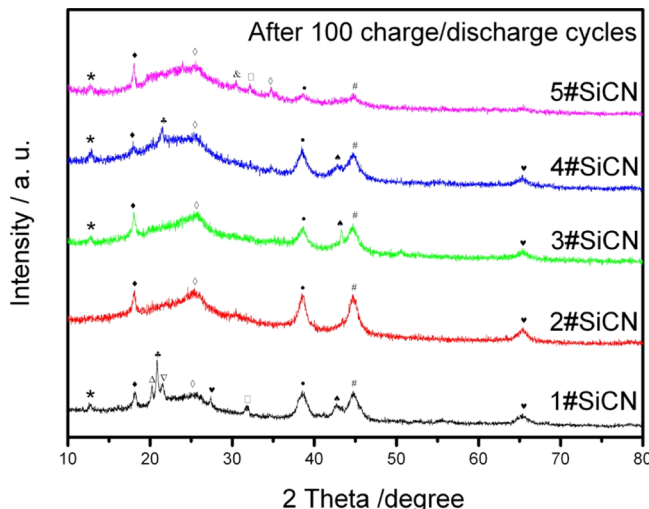


Figure 7. XRD patterns of 1–5#SiCN anodes after 100 charge/discharge cycles (*, LiC_{12} ; \blacklozenge , LiC_{16} ; \diamond , LiC_{24} ; ●, Li_2Si_5 ; #, Li_2Si_8 ; hearts, Si_3N_4 ; spades, Li_3Si_4 ; clubs, LiC_{40} ; Δ , Li_3Si_4 ; ∇ , $\text{Li}_{12}\text{Si}_7$; \square , LiC ; &, LiN_3).

XRD patterns of the 1–5#SiCN anodes after 100 charge/discharge cycles. There are many Li–C, Li–Si, Li–N, and Si–N phases in the 1–5#SiCN anodes after cycling, indicating that the original phases of Si_3N_4 , SiC, and graphite (observed by TEM in Figure 3e,f) in the SiCN anodes are transferred into the above-mentioned Li–C, Li–Si, and Li–N phase in the Li-ion insertion/extraction process. According to some references, Si_3N_4 phase is less reactive and irreversible in the lithiation/delithiation than the SiC phase.^{7,35,36} Therefore, the less Si_3N_4 phase in the electrode will decrease the capacity decay to some

Table 5. SiCN Samples Number and the Chemical Dosages for Synthesis

number/chemicals	1#SiCN	2#SiCN	3#SiCN	4#SiCN	5#SiCN
EDA	0.08 mol (4.76 g)	0.08 mol (4.76 g)	0.08 mol (4.76 g)	0.08 mol (4.76 g)	0.08 mol (4.76 g)
TEA	0.16 mol (14.90 g)	0.16 mol (14.90 g)	0.16 mol (14.90 g)	0.16 mol (14.90 g)	0.16 mol (14.90 g)
DCMVS	0.04 mol (5.20 g)	0.04 mol (5.20 g)	0.04 mol (5.20 g)	0.04 mol (5.20 g)	0.04 mol (5.20 g)
DCMS	0.04 mol (4.10 mL)				
DCDES		0.04 mol (6.00 mL)			
DCMOS			0.04 mol (11.40 mL)		
DCDPS				0.04 mol (8.40 mL)	
DODCS					0.04 mol (4.51 mL)
DCMVS/other/EDA/TEA (mol ratio)	1:1:2:4	1:1:2:4	1:1:2:4	1:1:2:4	1:1:2:4

(R₁, R₂=-H, -CH₃, -C₂H₅, -C₆H₅, -C₈H₁₇)

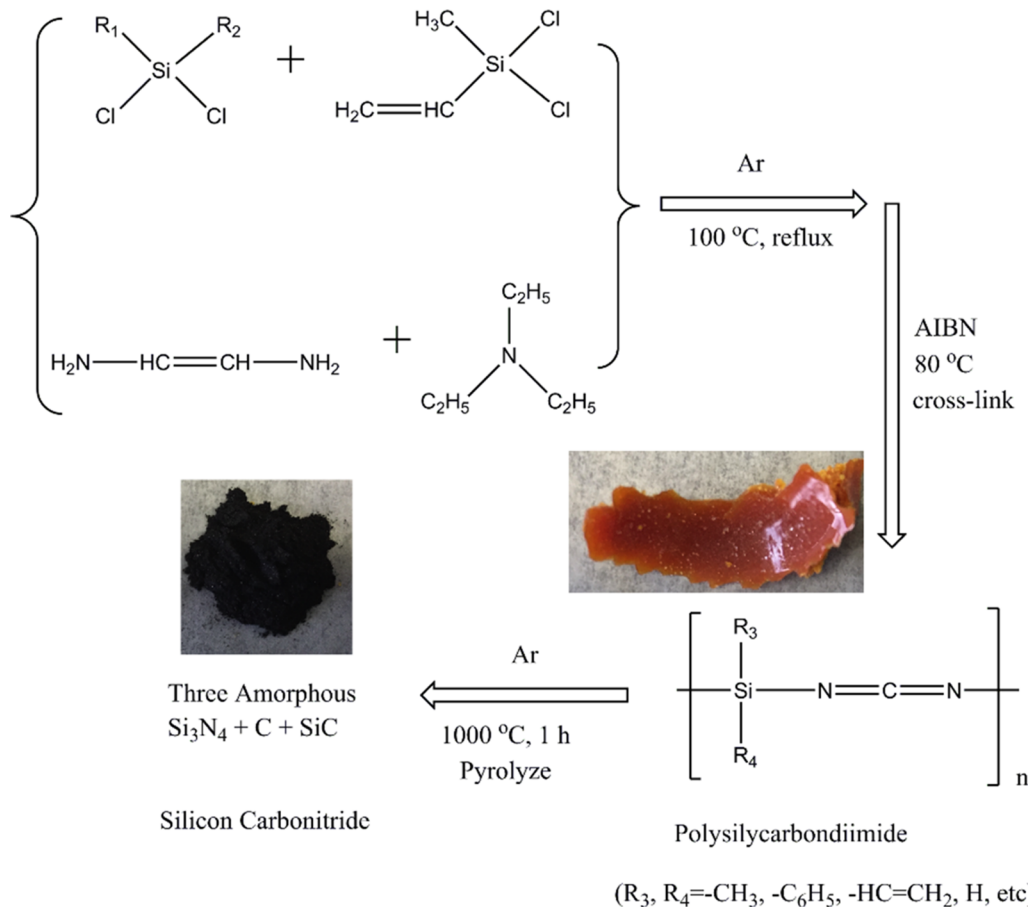


Figure 8. Preparation process of SiCN material.

extent. In Figure 7, the 5#SiCN anode has less Si₃N₄ phase among the five SiCN materials, which was also confirmed by the element analysis in Table 2 (the nitrogen ration is only 1.14 wt %). Thus, the less Si₃N₄ phase may the main reason for the best cycle stability of 5#SiCN among the five SiCN anodes.

In addition, the excellent electrochemical performance of 5#SiCN anodes is attributed to the composition of its polymer in the preparation. The carbon content in the 5#SiCN polymer is highest among all five SiCN polymers (Table 2). After pyrolysis, the carbon content is also the highest in the final product. As known, the carbon is very important for the cycle stability of the anode materials. Hence, adoption of a carbon-rich polymer for preparation is another key role to improve the cycle stability and decrease the capacity decay of SiCN anode.

3. CONCLUSIONS

The polymer-derived SiCN materials have been synthesized by the pyrolysis of five different polymers, polysilsilycarbonylidiimide. The SiCN materials are utilized as anodes for Li-ion batteries. Among the five SiCN samples, the 5#SiCN exhibits the best cycle stability, a high-rate performance, and Coulombic efficiency even at the low cutoff voltage of 0.01–1.0 V, which is qualified for use as the anode material in Li-ion full-cells. After 100 charge and discharge cycles, the specific delithiation capacity of 5#SiCN anode remains at 826.7 mA h g⁻¹. The 5#SiCN anode delivers above 550 mA h g⁻¹ even at the high current densities of 1.6 and 2 A g⁻¹. Except for the first two cycles, the Coulombic efficiency of all of the SiCN anodes is above 97%. The outstanding electrochemical performance of

5#SiCN anode is attributed to the formation of a stable and compact SEI layer on the anode surface anode, which protects the electrode from cracking during the charge/discharge cycle, resulting in decrease in capacity decay. Moreover, large amount of carbon component and less Si_3N_4 phase in the 5#SiCN material provide a much more electrochemically reactive and conductive environment in the SiCN structure, which benefits the lithiation/delithiation process. The results indicate that the following research should focus on the SiCN polymer composition, which has the important effect of further optimizing the carbon-rich SiCN structure on the corresponding pyrolyzed products for excellent electrochemical performance.

4. EXPERIMENTAL SECTION

4.1. Preparation of Polymer-Derived SiCN. The polymer-derived SiCN material was prepared by pyrolyzing a poly(silylcarbodiimide) precursor, which was synthesized by the aminolysis reaction of 1,2-ethylenediamine (EDA), triethylamine (TEA), and dichloromethylsilane (DCMS). The synthesis details are as follows: first, a solution of EDA (0.08 mol, 4.76 g) and TEA (0.16 mol, 14.90 g) in 100 mL toluene was placed in a 500 mL three-neck round-bottom flask fitted with a reflux condenser, a dropping funnel, and an argon inlet. The mixed solution was magnetically stirred. Then, dichloromethylvinylsilane (DCMVS, 0.04 mol, 5.20 g) and dichloromethylsilane (DCMS, 0.04 mol, 4.10 mL) in 50 mL toluene were then added slowly from the dropping funnel to this solution, and the reaction temperature was kept below 40 °C. The reaction mixture was refluxed at 60 °C for 40 min and then heated up to 100 °C and kept refluxed for 90 min. All of the reaction was carried out under an argon atmosphere. After the reaction mixture was cooled to room temperature, the precipitate (trimethylamine hydrochloride salt) was filtered off and the filtrate was rotary evaporated to remove the solvent and other volatile components. The remaining yellow oil was dried at room temperature under argon atmosphere overnight to obtain the precursor poly(silylcarbodiimide). The polymer precursor was cross-linked into a colloidal solid at 80 °C using 2,2-azobis-iso-butyronitrile (AIBN) as a radical initiator. After that, the cross-linked precursor was placed in an Al_2O_3 crucible and pyrolyzed in an alumina tube furnace under argon flow at 1000 °C for 1 h at a heating rate of 5 °C min⁻¹ to obtain SiCN bulk materials. Finally, the SiCN bulks were grinded and sieved with a 200 meshed standard sieve to obtain 1#SiCN powders.

With the same preparation process, dichlorodiethylsilane (DCDES), dichloromethyloctylsilane (DCMOS), dichlorodiphenylsilane (DCDPS), and di-*n*-octyldichlorosilane (DODCS) are replaced by dichloromethylsilane (DCMS) to obtain 2–5#SiCN powders, respectively. The dosages of the chemicals for the synthesis and the as-prepared SiCN products numbers are listed in Table 5. The preparation process of SiCN synthesis is shown in Figure 8. EDA, TEA, toluene, and AIBN were purchased from Jiangtian Tongyi Corp., China. DCMVS, DCMS, DCDES, DCMOS, DCDPS, and DODCS were purchased from Alfa-Aesar Corp., China. EDA, TEA, and toluene were removed of water by distillation before use. AIBN, DCMVS, DCMS, DCDES, DCMOS, DCDPS, and DODCS was used without purification.

4.2. Material Characterization. The morphologies of as-prepared SiCN materials were characterized with a scanning electron microscopy (SEM, JSM-7500F, the National Center for Electron Microscopy at Lawrence Berkeley National

Laboratory) and a transmission electron microscopy (TEM, FEI Tecnai G² F20, Philips, Tianjin Normal University). X-ray diffraction (XRD) measurements were taken on a Bruker D8A X-ray diffraction (Bruker, Germany) using Cu K α radiation ($\lambda = 0.154$ nm). Fourier transform infrared (FTIR) spectra were obtained on a Nicolet IR200 automatic infrared spectrometer (Thermo). Thermogravimetric analysis (TGA) was performed under argon using TGA Q600 system (TA Instruments). The sample was heated from room temperature to 1000 °C min⁻¹. Carbon and nitrogen elemental analyses were carried out with a Vario El Cube (Elementar Analysensystem GmbH, Germany). Raman measurements were performed on an Invia Raman microscope (Renishaw, England) with excitation laser beam wavelength of 514 nm.

4.3. Electrode Fabrication. The SiCN anodes were fabricated by mixing the SiCN powders with acetylene black (AB) and poly(vinylpyrrolidone) (PVP) binder in the weight ratio of 5:4:1. Dissolved in *N*-methyl-2-pyrrolidone (NMP), the mixtures were stirred at room temperature into a uniform slurry. Then, they were coated on an copper foil current collector with a Mitutoyo doctor blade and an Elcometer motorized film applicator. Mass loading of SiCN (the active material) was ~1.5 mg cm⁻². There was no modification of the current collector and the separator. After the NMP had dried off, the electrode laminated was further dried in vacuum at 50 °C for 24 h. From the SEM image of the cross-sectional view of the electrode in Figure S1 of the Supporting Information, the total thickness of the electrode could be observed as ~25 μm . Acetylene black (AB) was purchased from Denka, Japan. Poly(vinylpyrrolidone) (PVP) was purchased from Sigma-Aldrich. *N*-Methyl-2-pyrrolidone (NMP, anhydrous, 99.5 wt %) was purchased from Sigma-Aldrich.

4.4. Half-Cell Assembly. The 2325 coin cells (parts from National Research Council of Canada) were assembled in an argon-filled glovebox with an oxygen concentration of 0.1 ppm and a dew point of -70 °C. The SiCN electrode was punched to 9/16" outer diameter (OD) and the counter electrode was a lithium metal disk of 11/16" OD. The lithium-ion electrolyte was purchased from BASF, including 1.2 mol L⁻¹ LiPF₆ in ethylene carbonate and diethyl carbonate (EC/DEC = 3/7 w/w) containing 30 wt % fluoroethylene carbonate. The cell separator was polypropylene film (Celgard 2400) obtained from Celgard. Lithium foil was purchased from FMC-Lithium Corporation.

4.5. Full-Cell Assembly. The 2325 coin cells were assembled in an argon-filled glovebox with an oxygen concentration of 0.1 ppm and a dew point of -70 °C. The 5#SiCN material was used as a anode and the $\text{Li-Ni}_{0.6}\text{Co}_{0.2}\text{Mn}_{0.2}\text{O}_2$ (NCM cathode, type 622, SamSung) used as a cathode in the full-cell. The NCM cathode was fabricated by mixing the NCM powders with acetylene black (AB) and poly(vinylpyrrolidone) (PVP) binder in the weight ratio of 8:1:1. Dissolved in *N*-methyl-2-pyrrolidone (NMP), the mixtures were stirred at room temperature into a uniform slurry. Then they were coated on an copper foil current collector with a Mitutoyo doctor blade and an Elcometer motorized film applicator. Mass loading of NCM (the active material) was ~3.0 mg cm⁻². There was no modification of the current collector and the separator. After the NMP had dried off, the electrode laminated was further dried in vacuum at 50 °C for 24 h. The SiCN anode was fabricated to be used in half-cell electrode, punched to 11/16" OD. The NCM cathode was

punched to 9/16" OD. The lithium-ion electrolyte and cell separator were the same as the half-cells.

4.6. Cell Testing. Galvanostatic cycling tests were performed on a Maccor Series 4000 Battery Test System in a thermal chamber at 30 °C. As for the half-cell, the voltage window for cell test is 0.01–1.0 V; however, for the full-cell, the voltage window for cell test is 1.0–4.3 V. The calculation methods of current density and specific capacity are provided in the Supporting Information. Cyclic voltammetry (CV) test was performed on a Parstat 3000 galvanostat/potentiostat workstation (Princeton Applied Research, AMETEK) at a scan rate of 0.05 mV s⁻¹ at a potential interval 1.0 and 4.3 V. Electrochemical impedance spectroscopy (EIS) was also conducted on a Parstat 3000 workstation with a frequency range of 100 kHz to 10 mHz. The amplitude used for impedance measurement is 5 mV.

■ ASSOCIATED CONTENT

Supporting Information

The Supporting Information is available free of charge on the ACS Publications website at DOI: [10.1021/acsomega.7b01462](https://doi.org/10.1021/acsomega.7b01462).

Calculation methods of current density and specific capacity, Figure S1, SEM image of cross-sectional view of 5#SiCN anode; Figure S2, SEM images of 1#SiCN (a), 2#SiCN (b), 3#SiCN (c), 4#SiCN (d), and 5#SiCN (e) materials; Figure S3, Graphs of the Coulombic efficiency vs cycle number for 1–5#SiCN anodes ([PDF](#))

■ AUTHOR INFORMATION

Corresponding Authors

*E-mail: hxyfy@mail.tjnu.edu.cn (Y.F.).

*E-mail: xfl2011@hotmail.com (X.L.).

ORCID

Yan Feng: [0000-0003-4037-0674](https://orcid.org/0000-0003-4037-0674)

Xifei Li: [0000-0002-4828-4183](https://orcid.org/0000-0002-4828-4183)

Notes

The authors declare no competing financial interest.

■ ACKNOWLEDGMENTS

This work was supported by the National Natural Science Foundation of China (Nos. 21103124 and 51572194) and the Academic Innovation Funding for the Middle-age and Young Professors of Tianjin Normal University (Nos. 52XC1502 and 52XC1404). Dr. Yan Feng is supported by the China Scholarship Council (No. 201408120022).

■ REFERENCES

- (1) Sheng, T.; Xu, Y.-F.; Jiang, Y.-X.; Huang, L.; Tian, N.; Zhou, Z.-Y.; Broadwell, I.; Sun, S.-G. Structure design and performance tuning of nanomaterials for electrochemical energy conversion and storage. *Acc. Chem. Res.* **2016**, *49*, 2569–2577.
- (2) Seh, Z. W.; Sun, Y.; Zhang, Q.; Cui, Y. Designing high-energy lithium-sulfur batteries. *Chem. Soc. Rev.* **2016**, *45*, 5605–5634.
- (3) Goodenough, J. B.; Park, K.-S. The Li-ion rechargeable battery: a perspective. *J. Am. Chem. Soc.* **2013**, *135*, 1167–1176.
- (4) Agostini, M.; Brutti, S.; Hassoun, J. High voltage Li-ion battery using exfoliated graphite/graphene nanosheets anode. *ACS Appl. Mater. Interfaces* **2016**, *8*, 10850–10857.
- (5) Niehoff, P.; Passerini, S.; Winter, M. Interface investigations of a commercial lithium ion battery graphite anode material by sputter depth profile X-ray photoelectron spectroscopy. *Langmuir* **2013**, *29*, 5806–5816.
- (6) Colombo, P.; Mera, G.; Riedel, R.; Soraru, G. D. Polymer-derived ceramics: 40 years of research and innovation in advanced ceramics. *J. Am. Ceram. Soc.* **2010**, *93*, 1805–1837.
- (7) Mera, G.; Navrotsky, A.; Sabyasachi, S.; Kleebe, H.-J.; Riedel, R. Polymer-derived SiCN and SiOC ceramics – structure and energetics at the nanoscale. *J. Mater. Chem. A* **2013**, *1*, 3826–3836.
- (8) Liebau-Kunzmann, V.; Fasel, C.; Kolb, R.; Riedel, R. Lithium containing silazanes as precursors for SiCN:Li ceramics – A potential material for electrochemical applications. *J. Eur. Ceram. Soc.* **2006**, *26*, 3897–3901.
- (9) Gummán, S.; Nestle, N.; Liebau-Kunzmann, V.; Riedel, R. Investigations of Li-containing SiCN(O) ceramics via ⁷Li MAS NMR. *Solid State Nucl. Magn. Reson.* **2007**, *31*, 82–90.
- (10) Su, D.; Li, Y.-L.; Feng, Y.; Jin, J. Electrochemical properties of polymer-derived SiCN materials as the anode in lithium ion batteries. *J. Am. Ceram. Soc.* **2009**, *92*, 2962–2968.
- (11) Feng, Y. Electrochemical properties of heat-treated polymer-derived SiCN anode for lithium ion batteries. *Electrochim. Acta* **2010**, *55*, 5860–5866.
- (12) Graczyk-Zajac, M.; Reinold, L. M.; Kaspa, J.; Sasikumar, P. V. W.; Soraru, G.-D.; Riedel, R. New insights into understanding irreversible and reversible lithium storage within SiOC and SiCN ceramics. *Nanomaterials* **2015**, *5*, 233–245.
- (13) Sanchez-Jimenez, P. E.; Rishi, R. Lithium insertion in polymer-derived silicon oxycarbide ceramics. *J. Am. Ceram. Soc.* **2010**, *93*, 1127–1135.
- (14) Fukui, H.; Harimoto, Y.; Akasaka, M.; Eguchi, K. Lithium species in electrochemically lithiated and delithiated silicon oxycarbides. *ACS Appl. Mater. Interfaces* **2014**, *6*, 12827–12836.
- (15) David, L.; Bernard, S.; Gervais, C.; Miele, P.; Singh, G. Facile synthesis and high rate capability of silicon carbonitride/boron nitride composite with a sheet-like morphology. *J. Phys. Chem. C* **2015**, *119*, 2783–2791.
- (16) Nowak, A. P.; Wicikowska, B.; Lisowska-Oleksiak, A. New ceramic materials derived from pyrolyzed poly(1,2-dimethylsilazane) and starch as a potential anode for Li-ion batteries. *Solid State Ionics* **2014**, *263*, 131–139.
- (17) Feng, Y.; Feng, N.-N.; Du, G.-X. Preparation and electrochemical performance of polymer-derived SiCN-graphite composite as anode material for lithium ion batteries. *Int. J. Electrochem. Sci.* **2012**, *7*, 3135–3140.
- (18) Feng, Y.; Du, G.-X.; Zhao, X.-J.; Yang, E.-C. Preparation and electrochemical performance of SiCN-CNTs composite anode material for lithium ion batteries. *J. Appl. Electrochem.* **2011**, *41*, 999–1002.
- (19) Feng, Y.; Feng, N.; Wei, Y.; Bai, Y. Preparation and improved electrochemical performance of SiCN-graphene composite derived from poly(silylcarbodiimide) as Li-ion battery anode. *J. Mater. Chem. A* **2014**, *2*, 4168–4177.
- (20) Kolb, R.; Fasel, C.; Liebau-Kunzmann, V.; Riedel, R. SiCN/Ceramic composite as anode material for lithium ion batteries. *J. Eur. Ceram. Soc.* **2006**, *26*, 3903–3908.
- (21) Ionescu, E.; Francis, A.; Riedel, R. Dispersion assessment and studies on AC percolative conductivity in polymer-derived Si-C-N/CNT ceramic nanocomposites. *J. Mater. Sci.* **2009**, *44*, 2055–2062.
- (22) Graczyk-Zajac, M.; Fasel, C.; Riedel, R. Polymer-derived-SiCN ceramic/graphite composite as anode material with enhanced rate capability for lithium ion batteries. *J. Power Sources* **2011**, *196*, 6412–6418.
- (23) Bhandavat, R.; Singh, G. Improved electrochemical capacity of precursor-derived Si(B)CN-carbon nanotube composite as Li-ion battery anode. *ACS Appl. Mater. Interfaces* **2012**, *4*, 5092–5097.
- (24) Wilamowska, M.; Graczyk-Zajac, M.; Riedel, R. Composite materials based on polymer-derived SiCN ceramic and disordered hard carbons as anodes for lithium-ion batteries. *J. Power Sources* **2013**, *244*, 80–86.
- (25) Graczyk-Zajac, M.; Gabriela, M.; Kaspar, J.; Riedel, R. Electrochemical studies of carbon-rich polymer-derived SiCN ceramics

as anode materials for lithium-ion batteries. *J. Eur. Ceram. Soc.* **2010**, *30*, 3235–3243.

(26) Kaspar, J.; Mera, G.; Nowak, A. P.; Graczyk-Zajac, M.; Riedel, R. Electrochemical study of lithium insertion into carbon-rich polymer-derived silicon carbonitride ceramics. *Electrochim. Acta* **2010**, *56*, 174–182.

(27) Mera, G.; Riedel, R.; Poli, F.; Müller, K. Carbon-rich SiCN ceramics derived from phenyl-containing poly(silylcarbodiimides). *J. Eur. Ceram. Soc.* **2009**, *29*, 2873–2883.

(28) Reinold, L. M.; Graczyk-Zajac, M.; Gao, Y.; Mera, G.; Riedel, R. Carbon-rich SiCN ceramics as high capacity / high stability anode material for lithium-ion batteries. *J. Power Sources* **2013**, *236*, 224–229.

(29) Reinold, L. M.; Yamada, Y.; Graczyk-Zajac, M.; Munakata, H.; Kanamura, K.; Riedel, R. The influence of the pyrolysis temperature on the electrochemical behavior of carbon-rich SiCN polymer-derived ceramics as anode materials in lithium-ion batteries. *J. Power Sources* **2015**, *282*, 409–415.

(30) Baek, S.-H.; Reinold, L. M.; Graczyk-Zajac, M.; Riedel, R.; Hammerath, F.; Büchner, B.; Grafe, H.-J. Lithium dynamics in carbon-rich polymer-derived SiCN ceramics probed by nuclear magnetic resonance. *J. Power Sources* **2014**, *253*, 342–348.

(31) Liu, G.; Kaspar, J.; Reinold, L. M.; Graczyk-Zajac, M.; Riedel, R. Electrochemical performance of DVB-modified SiOC and SiCN polymer-derived negative electrodes for lithium-ion batteries. *Electrochim. Acta* **2013**, *106*, 101–108.

(32) Chen, Y.; Li, C.; Wang, Y.; Zhang, Q.; Xu, C.; Wei, B.; An, L. Self-assembled carbon-silicon carbonitride nanocomposites: high-performance anode materials for lithium-ion batteries. *J. Mater. Chem.* **2011**, *21*, 18186–18190.

(33) Feng, Y.; Zhang, Y.; Wei, Y.; Song, X.; Fu, Y.; Battaglia, V. S. A ZnS nanocrystal/reduced graphene oxide composite anode with enhanced electrochemical performances for lithium-ion batteries. *Phys. Chem. Chem. Phys.* **2016**, *18*, 30630–30642.

(34) Feng, Y.; Zhang, Y.; Song, X.; Wei, Y.; Battaglia, V. S. Facil hydrothermal fabrication of ZnO-graphene hybrid anode materials with excellent lithium storage properties. *Sustainable Energy Fuels* **2017**, *1*, 767–779.

(35) Feng, N.; Feng, Y.; Wei, Y.; Zhou, X. Preparation and electrochemical performance of a porous polymer-derived silicon carbonitride anode by hydrofluoric acid etching for lithium ion batteries. *RCS Adv.* **2014**, *4*, 23694–23702.

(36) Feng, Y.; Wei, Y.; Jia, Z.; Zhang, Y.; Battaglia, V.; Liu, G. Polymer-derived and sodium hydroxide-treated silicon carbonitride material as anodes for high electrochemical performance Li-ion batteries. *ChemistrySelect* **2016**, *1*, 309–317.

(37) Liang, J.; Li, X. N.; Hou, Z.; Zhang, W.; Zhu, Y.; Qian, Y. A deep reduction and partial oxidation strategy for fabrication of mesoporous Si anode for lithium ion batteries. *ACS Nano* **2016**, *10*, 2295–2304.

(38) Luo, L.; Zhao, P.; Yang, H.; Liu, B.; Zhang, J. G.; Cui, Y.; Yu, G.; Zhang, S.; Wang, C. M. Surface coating constraint induced self-discharging of silicon nanoparticles as anodes for lithium ion batteries. *Nano Lett.* **2015**, *15*, 7016–7022.